Received: 21 October 2020 | Revised: 24 November 2020 | Accepted: 14 December 2020
DOI: 10.1002/aoc.6137

FULL PAPER

Applied Organometallic Chemistry WILEY

Synthesis, characterization and evaluation of novel ferrocenylmethylamine derivatives as cytotoxic agents

Chirag J. Savani[1] | **Hetal Roy**[1] | **Sanjay K. Verma**[1] | **Dushyanth R. Vennapu**[2] | **Vinay K. Singh**[1]

[1]Department of Chemistry, Faculty of Science, The M. S. University of Baroda, Vadodara, India

[2]Department of Pharmaceutical Chemistry, KLE University College of Pharmacy, Belagavi, India

Correspondence
Vinay K. Singh, Department of Chemistry, Faculty of Science, The M. S. University of Baroda, Vadodara-390002, India.
Email: vinay.singh-chem@msubaroda.ac.in

Funding information
Science and Engineering Research Board, Grant/Award Number: EMR/2016/003172

The present report describes a new series of amide functionalized 2^0- and 3^0-aminomethylferrocene derived from ferrocenylmethylamine. The compounds 1a-5a and 1b-5b were characterized by microanalysis, ^1H, ^{13}C NMR, UV–visible, fluorescence, FTIR, thermogravimetric and crystallographic techniques. The X-ray analysis demonstrated the ability of these molecules to form various intermolecular hydrogen bonding interactions, as verified by Hirshfeld surface analysis. All the compounds were evaluated against MCF 7, IMR 32, HepG2 and immortal L132 cell lines by MTT assay and the results were compared with cisplatin. Interestingly, many compounds were very active against all the investigated cell lines and proved to be more potent as cytotoxic agents than cisplatin. The western blot, gene expression, mitochondrial membrane potential and flow cytometry study were used to investigate the mode of action of these derivatives as antitumor agents. The results showed apoptotic property of the compounds by modulating inflammatory pathway against human tumor cells of different origin. We performed the density functional theory calculations and molecular docking to rationalize the experimental results.

KEYWORDS
amide functionalized 2^0- and 3^0-aminomethylferrocene, anticancer, apoptosis, molecular docking, X-ray diffraction

1 | INTRODUCTION

The interest in the ferrocene[1] and its new derivatives has been continued due to their myriad of technological applications. The intriguing redox properties of ferrocenes led to applications in coordination chemistry,[2] inorganic materials,[3] molecular wires, sensors,[4] macrocages,[5] clusters growth,[6], catalysis[7] and in medicinal research.[8] Particularly, the development of new molecules that induce apoptosis and DNA fragmentation is crucial for the discovery and development of novel anticancer agents.[9] It has been reported that ferrocene involves in the generation of reactive oxygen species (ROS) within the cells, improvement of biological activity, overcome resistance barriers, lipophilic character, redox activity and enabling easier passage through cell membranes.[10] Despite the nontoxic nature of ferrocene, its stability in aqueous and aerobic media, many ferrocenyl derivatives exhibit significant anticancer, antibacterial, antiparasi tic, antifungal and other biological activities.[11] Particularly, Jaouen et al. has developed more efficient ferrocifen type anticancer agents as analogues of the tamoxifen with innovative

Dedicated to Professor Pradeep Mathur, IIT Bombay, on the occasion of his 65th Birthday.

mechanisms of action.[12] Further reports suggest that incorporating amino groups into the molecular framework helps in an active transport process via the formation of organic cation transporters and is responsible for the improved biological activity.[13] For instance, covalently linkage of N,N-dimethyl tertiary amino group to celastrol (CTA) exhibited excellent cellular uptake efficiency in both rat pancreatic acinar cell line (AR42J) and human pulmonary alveolar epithelial cell line (A549).[14] Moreover, there are many drugs available in the market namely, penicillin G, mociobemide, acetazolamide, trimethobenzamide and so forth, which contain amide linkage in the nucleus and possesses various therapeutic activities.[15] Professor Jianjun Chen and his group recently reported several diarylmethane amides displaying excellent neuroprotective and anticancer activities.[15]

In light of the above considerations and the fact that amines are highly essential fine and bulk chemicals used in chemistry, medicine, biology and materials,[16] we began optimizing the reaction conditions to obtain the new ferrocenylmethylamine derivatives. Synthetically challenging derivatives ca 2-(ferrocenylmethylamino)-N-alkylacetamides 1a-5a and 2, 2′-(ferrocenylmethylazanediyl) bis(N-alkylacetamides) 1b-5b (Scheme 1) were derived selectively and characterized for their apoptotic potentials against human cancer cell lines. We performed inflammatory pathway study and detailed molecular mechanism to understand these compounds as promising anticancer agents. X-ray crystallography was used to elucidate the openings of secondary interactions provided using scaffold substitutions. We attempted to explore the apoptotic regulatory influence of various substitution patterns at the amidic nitrogen on TNFα inhibition through molecular docking. The synthesized inhibitors contained an optimal substitution of *p*-methybenzyl in 4b and *p*-methoxybenzyl in 5b ligands, allowing us to probe the secondary interactions of the modified amidic nucleus with the TNFR1 protein.

2 | RESULTS AND DISCUSSION

2.1 | Synthesis and characterization

It is worth noting that ferrocenylmethyamine did not react with α-chloroamide precursors CA1-CA5, unlike others[17] to give desired products. The α-chloroamide precursors CA1-CA5 were then converted to α-iodoamide precursors IA1-IA5, which were indeed reacted with ferrocenylmethyamine to give a new series of amide functionalized ferrocenylmethylamine derivatives 1a-5a, 1b-5b in moderate to high yield (Scheme 2). Using the optimized reaction conditions, we tested the scope of this procedure and established the best reaction conditions for the selective formation of mono-amide functionalized 2^0-aminomethylferrocene 1a-5a and diamide functionalized 3^0-aminomethylferrocene 1b-5b, which contain promising ferrocenyl, amino and amido groups in the molecular framework.

Newly synthesized amide functionalized 2^0-ferrocenemethylamines 1a-5a were isolated in a thick liquid form while 3^0-aminomethylferrocenes 1b-5b were isolated as solid. All the ligands are fairly soluble in common organic solvents and found to be stable in pure state and in the solution over a period of days. The compositions and phase purity of the samples were confirmed by microanalysis and by ^{1}H and ^{13}C

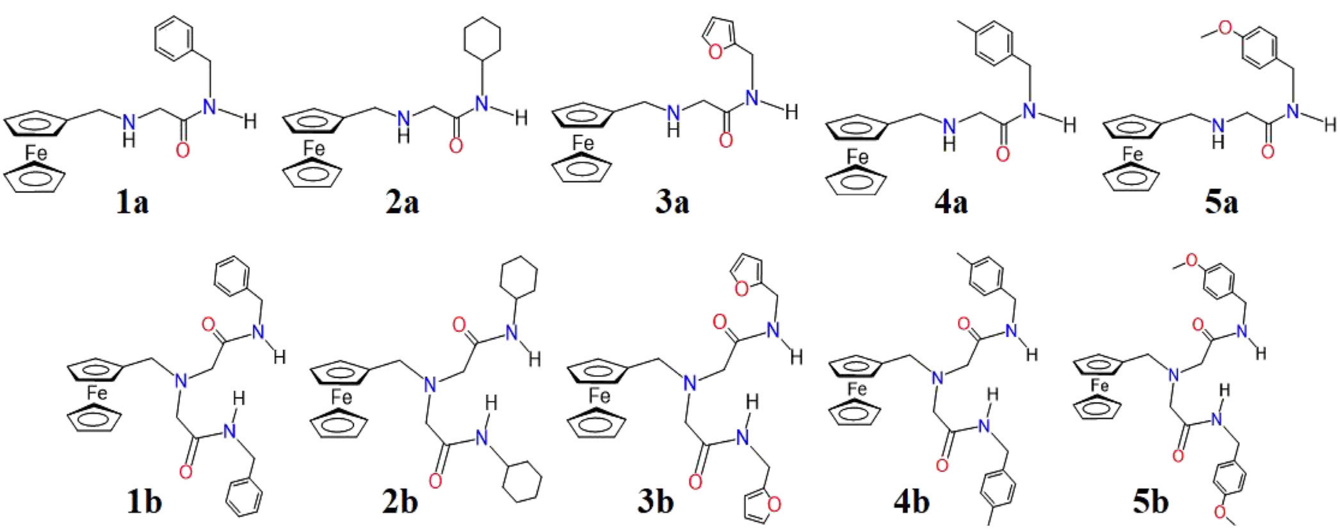

SCHEME 1 List of newly synthesized ligands under investigation

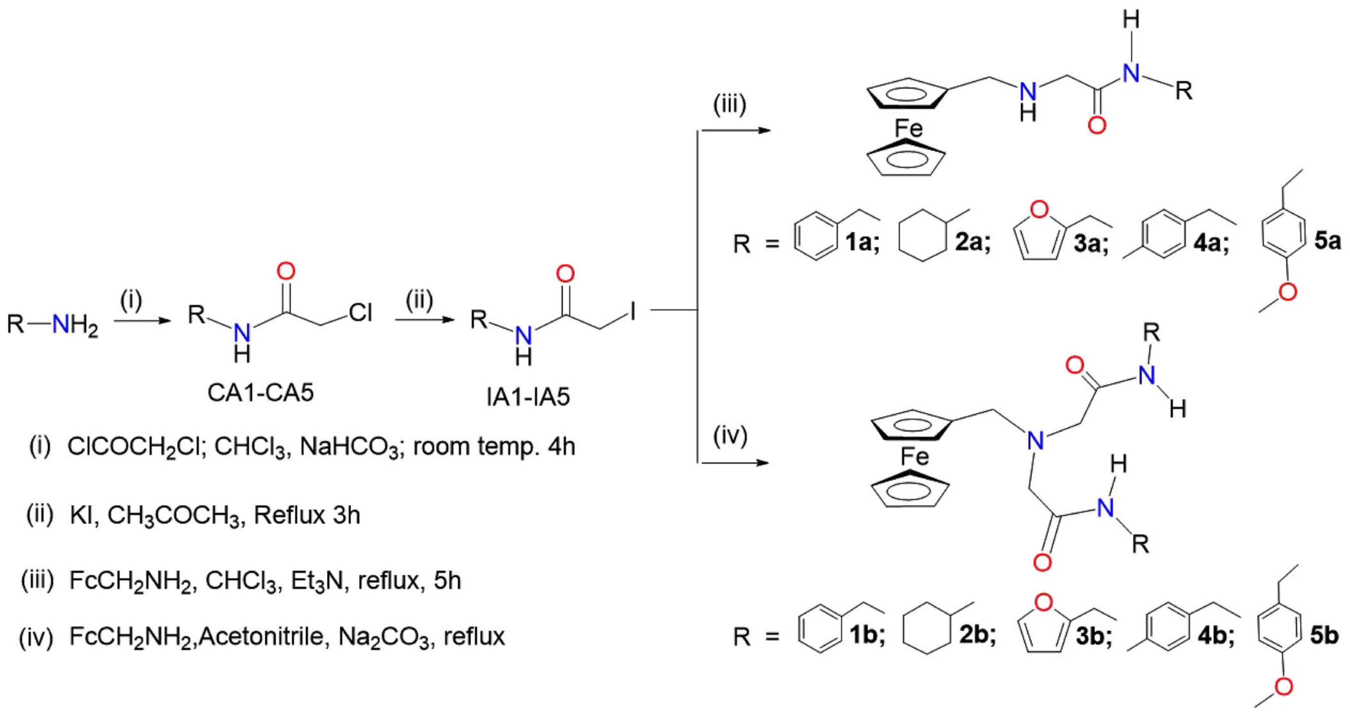

SCHEME 2 General synthetic strategies adopted for 2-(ferrocenylmethylamino)-N-alkylacetamide (1a-5a) and 2, 2′-(ferrocenylmethylazanediyl)-bis-(*N*-alkylacetamide) (1b-5b)

spectroscopy. The NMR (Figures S1–S20, electronic supplementary information [ESI]) and IR spectra (Figures S21–S30, ESI) gives confirmation of various groups namely, ferrocenyl, amino-, amido-, alkyl- and aryl present in 1a-5a, 1b-5b. The assigned IR and NMR data are summarized in the experimental section. Ferrocene appears in the range of 3.98–4.43 ppm in the ^{1}H NMR spectrum of 1a-5a, 1b-5b. Notably, di-amide functionalized 3^{0}-aminomethylferrocenes 1b-5b show two different CO stretching frequencies in 1681–1640 cm^{-1} region (Figures S22, S24, S26, S28 and S30, ESI) due to the involvement of one of the amidic CO in intermolecular hydrogen bonding and noninvolvement other amidic CO in such interactions as revealed by X-ray diffraction study (vide infra). The UV–visible spectral spectrum of all ligand gives a high intensity absorption bands in the region of 300–324 nm (Figure 1/Figure S31, ESI), which is mainly attributed to the locally excited $n \rightarrow \pi^*$ transitions. A broad, low-intensity band observed in the 430- to 439-nm region attributable to metal (LMCT) charge transfer transitions, a characteristic feature of attached ferrocene moiety.[11]

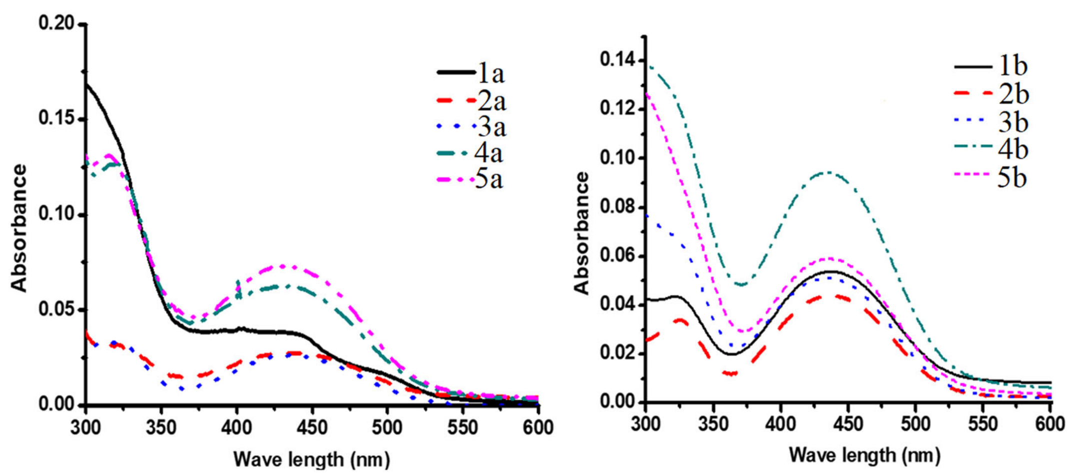

FIGURE 1 UV–visible absorption spectrum of the compounds under investigation at room temperature in 10^{-5} M CH_3CN

The majority of the ligands fluoresce in the visible region, upon excitation in the ultraviolet region with a concomitant Stokes shift of 60–100 nm (Figure S32 and Table S1, ESI). The DTA curves (Figure 2) show an endothermic peak at 142.8°C (for 1b), 153. 7°C (for 2b), 131.7°C (for 3b), 123.3°C (for 4b) and 170.0°C (for 5b), respectively, without any mass loss on DTG curves and these peaks attributes to the melting point of the ligands. Notably, TGA curves of 1b-5b essentially show one-step decomposition in the 200–550°C temperature range with weight loss of 76.4%, 75.4%, 60%, 64.4% and 67.0% respectively, leaving the residue of Fe_2O_3 in each case (Table 1). The ability of these ligands to form Fe_2O_3 may be a factor for their enhanced anti-proliferative activity at low micro molar concentration (vide infra). Evidently, the possible toxicity study of Fe_2O_3 in human cells, including blood lymphocytes indicated that Fe_2O_3 significantly reduced the cell viability and at different concentrations, Fe_2O_3 NPs affect cellular glutathione (GSH) level and cause oxidative stress in human lymphocytes.[18]

2.2 | X-ray crystallographic study

The liquid samples of 1a and 3a, which contain 2^0 amine moieties, were crystallized in the salt form in triclinic P-1 (1a.*2HI.H₂O*) and monoclinic Cc (3a.*CH_3COOH*) space groups, respectively. Solid samples crystallize in monoclinic $P2_1/c$ (3b, 4b) and triclinic P-1 (5b) centrosymmetric space groups. X-ray crystal structure shows one complete molecule in their asymmetric units, except 1a.*$2HI.H_2O$* and 5b, which contains two complete molecules in their asymmetric units. The *ORTEP* view at 50% probability for these compounds is shown in Figure 3. Details about data collection, refinement and structure solution are recorded in (Table S2, ESI) and selected geometrical parameters are in the beneath of Figure 3.

The structural parameters such as bond lengths and bond angles are found to be consistent with the literature.[10,19] The density functional calculations have appeared in good support to the experimentally determined similar parameters (ESI). Notably, X-ray crystallography revealed the propensity of amidic and amine groups of newly synthesized amines to form intermolecular hydrogen bonding (Figures 4 and S33, ESI).

Hirshfeld surface analysis was employed to understand and quantify the noncovalent interactions, for example, hydrogen bonding, π-forces and the details are summarized in the ESI. The fingerprint plots of close contacts (Figure S52, ESI) confirm both strong and weak intermolecular interactions. The relative contributions of the intermolecular contacts in 1a, 3a, 3b, 4b and 5b are given in Table S17 and Figure S53. This indicates the ability of these molecules to offer secondary interaction in the biological system, required for cell growth inhibition. To reveal the inhibitory influence of various substituents at the amidic scaffold of 1a-5a and 1b-5b, interactions of these with 1tnf protein was carried

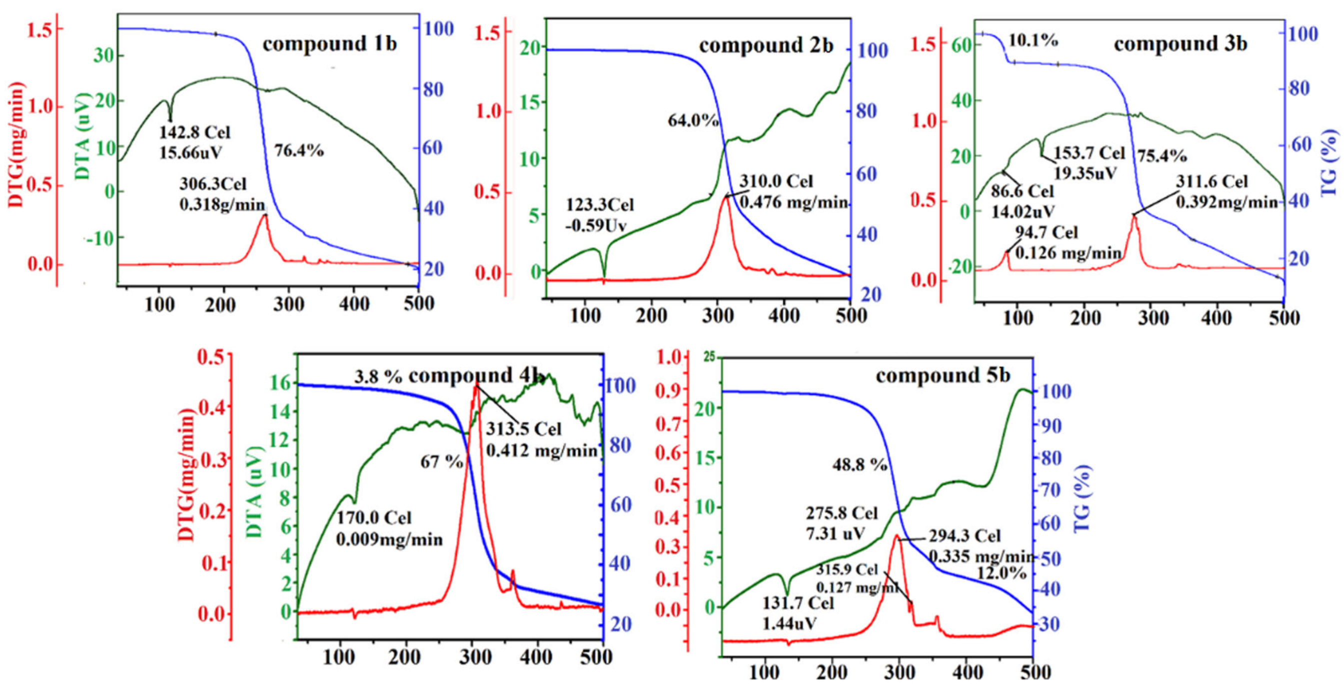

FIGURE 2 TG/DTA curves for the ligands 1b-5b

TABLE 1 TGA results for the ligands 1b-5b

ligand	T (°C) in DTA	T (°C) in TGA	residue wt. observed (Calcd.) (%)	expected product of decomposition
1b	142.8	220	0.0 (phase transition)	—
	—	220–550	23.6 (31.4)	Fe_2O_3
2b	153.7	200	0.0 (phase transition)	—
	—	200–550	24.6 (32.5)	Fe_2O_3
3b	131.7	200	0.0 (phase transition)	—
	—	200–550	39.2 (32.8)	Fe_2O_3
4b	123.3	210	0.0 (phase transition)	—
	—	210–550	36 (29.8)	Fe_2O_3
5b	170.0	180	0.0 (phase transition)	—
	—	200–550	33 (28.2)	Fe_2O_3

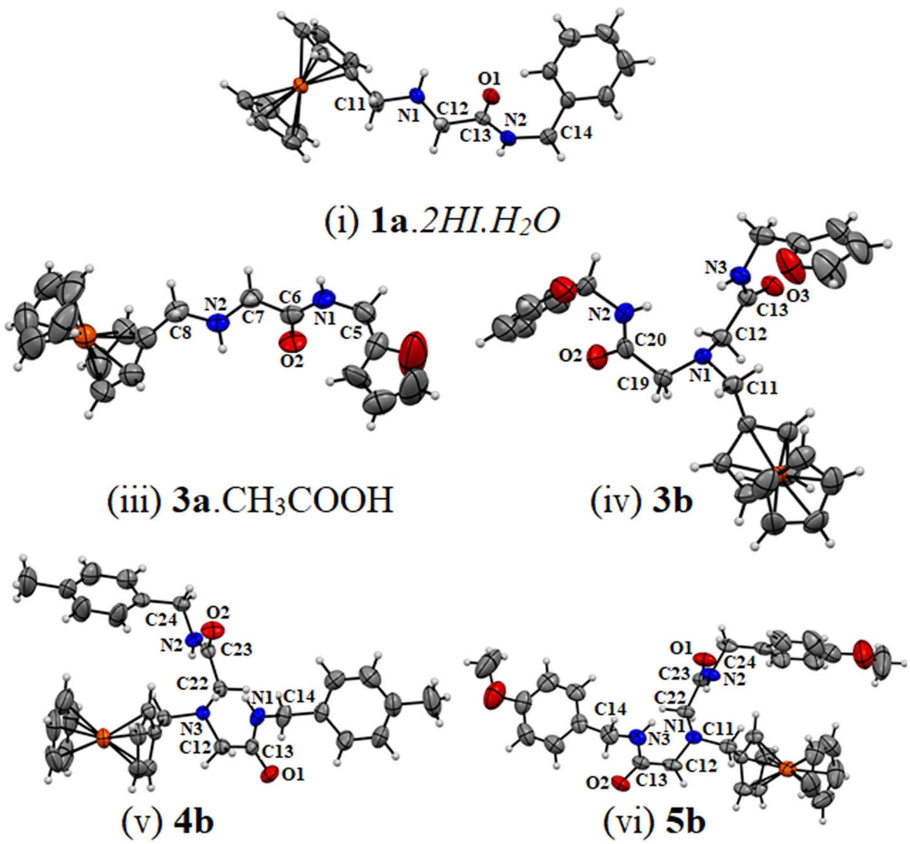

FIGURE 3 The ORTEP diagram with partial atom numbering showing 50% probability ellipsoid; (hydrogen atoms and solvent molecules from 1a and 3a are removed for clarity) for (i) **1a**.*2HI.H₂O*, selected bond lengths (Å): N1–C11, 1.468(6); N1–C12, 1.482(5); C13–C12, 1.509(6); C13–O1, 1.230(5); C13–N2, 1.321(6); (ii) **3a**.*CH_3COOH*, selected bond lengths (Å): N2–C8, 1.506 (11); N2–C7, 1.507(10); C6–C7, 1.520 (12); O2–C6, 1.235(10); N1–C6, 1.326 (11); (iii) **3b**, selected bond lengths (Å): N2–C21, 1.451(7); N2–C20, 1.338(8); O2–C20, 1.215(7); C19–C20, 1.511(8); N1–C19, 1.452(7); (iv) **4b**, selected bond lengths (Å): N2–C24, 1.447(4); N2–C23, 1.318(4); O2–C23, 1.234(3); C23–C22, 1.510(4); N3–C22, 1.461(3); (v) **5b**, selected bond lengths (Å): C14–N3, 1.460(7); N3–C13, 1.345(7); O2–C13, 1.221(6); C12–C13, 1.510(8); N1–C12, 1.462(6)

out using molecular docking for further study on lead molecules.

2.3 | Inhibitory activity and structure activity relationships (SARs)

We first set out to systematically examine the influence of diverse set of simple substituents at amidic nucleus on cytotoxic activity of 1a-5a and 1b-5b. The cytotoxic potential of these amide functionalized ferrocenenylmethylamine derivatives against selected cell lines is presented in Table 2 (Figure S34, ESI). Table 2 revealed that bis-amide inhibitors 1b-5b show improved cytotoxicity profile as compared to mono-amide inhibitors 1a-5a, against various cell lines due to availability of more binding sites (amidic group). Evidently, the introduction of an optimal substituents *p*-methylbenzyl and *p*-methoxybenzyl at the amidic nitrogen of bis-amide inhibitors 4b and 5b, respectively, gave a remarkable increase in cytotoxicity against several cell lines. For instance, in comparison to the reference drug cisplatin,

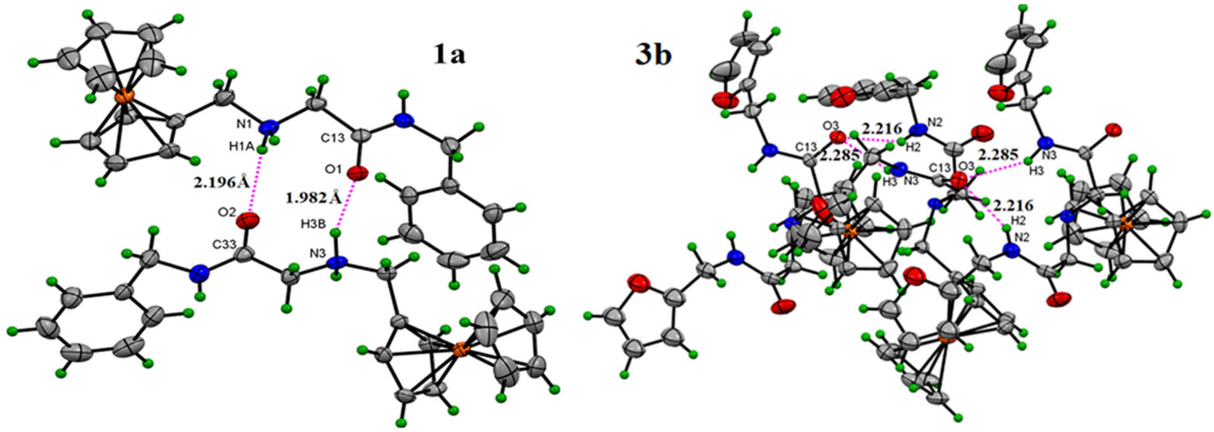

FIGURE 4 Propensity of amines 1a and 3b to form intermolecular H bonding

TABLE 2 In vitro cytotoxicity on cell line after 24 h of exposure of 2-(ferrocenylmethylamino)-N-alkylacetamide (1a-5a), 2, 2′-(ferrocenylmethylazanediyl)bis(*N*-alkylacetamide) (1b-5b)

		IC_{50} values (μM)			
	Ligand	MCF 7	IMR 32	L132	HepG2
1	1a	41.45 ± 0.22	35.45 ± 0.11	91.80 ± 0.07	13.19 ± 0.17
2	1b	23.63 ± 0.12	52.11 ± 0.11	22.37 ± 0.13	7.25 ± 0.11
3	2a	15.54 ± 0.54	53.20 ± 0.15	43.74 ± 0.08	25.38 ± 0.21
4	2b	10.49 ± 0.37	31.96 ± 0.20	71.68 ± 0.01	14.60 ± 0.08
5	3a	50.42 ± 0.43	30.35 ± 0.07	94.30 ± 0.14	33.84 ± 0.37
6	3b	12.89 ± 0.33	19.14 ± 0.20	93.79 ± 0.12	13.74 ± 0.05
7	4a	29.07 ± 0.09	16.17 ± 0.19	13.77 ± 0.01	24.14 ± 0.22
8	4b	11.49 ± 0.07	10.39 ± 0.30	19.10 ± 0.12	25.25 ± 0.08
9	5a	15.60 ± 0.19	17.55 ± 0.19	18.74 ± 0.24	16.83 ± 0.09
10	5b	2.10 ± 0.41	16.95 ± 0.15	13.56 ± 0.07	8.66 ± 0.21
11	Cisplatin	32.41 ± 1.5	29.6 ± 1.26	21.4 ± 2.2	24.3 ± 1.7

Note: Values are represented as mean ± SEM.

inhibitors 5b and 4b showed ~15 folds and ~3 fold better inhibition against MCF 7, respectively. Notably, the introduction of benzyl substituent at the amidic nitrogen of bis-amide inhibitor 2b gave similar result to that of 4b against MCF 7. Inhibitors 4b and 5b showed ~3–2 folds better activity against IMR 32 than the reference. Against the hepatocellular carcinoma HepG2 cell line, inhibitor 5b showed comparable activity to that of 1b. Although, inhibitors 1b, 2b and 3b have shown better potency than the reference drug, however, the highest activity against HepG2 was observed for 5b and 1b which contain *p*-methoxybenzyl and benzyl substituents at amidic nitrogen. The IC_{50} values of synthesized inhibitors were found to be most effective on HepG2 amongst all the investigated cell line cells.

Notably, Tyr119 was identified as a common binding site for all the inhibitors, but on substitution of amidic scaffold with *p*-methoxybenzyl, switches the inhibitor binding mode of 5b to Gly121 with TNFR1, which authenticate 5b as potent antiproliferative agent. To shed more light on the experimental observations, the geometry of all the ligands has been optimized by a DFT level calculations (Figure S50 and Tables S6–S16). The molecular electrostatic potential (Figure S51, ESI) of all the ligands clearly demonstrates that the presence of polar amide subunits which are indeed projected towards the outside. This provides H-bond donor-acceptor sites to facilitate the interactions with biomolecules, leading to the effective cellular membrane transportation causing increased concentration of complexes at the site of action. Moreover, the presence of bulkier *p-methoxybenzyl* substituents probably enhances the lipophilicity resulting in greater cellular accumulation, responsible for its better activity.

The obtained IC_{50} values for herein studied ferrocene ligands (except some) are more effective than cisplatin on different human cancer cell line. For analysis of cytotoxicity, uptake of the molecule by the cell is an important process. Hereby with aim to identify the lead ligands for their drug likeness, we studied the molecular properties of ligands by ADMET analysis and screened by Lipinski and Veber filters.[20] Ligands with optimum cell permeability should follow the criteria PSA < 140 Å2 and AlogP98 < 5. All of the ligands showed the best fit of the proposed model (Table S4 and Figures S46 and S47, ESI). Furthermore, the quantitative structure, toxicity relationship (QSTR) was performed to validate the toxic potentials of the lead ligands. Many of the compounds in the present series showed anticancer activity in low micromolar concentrations, which is indeed comparable with the activity of several high molecular weight organometallic compounds, recently reported in the literature elsewhere (Table S3, ESI). Notably, some of the compounds showed better activity than the activity of several ferrocence-glycine/L-alanine hybrid compounds, recently reported in the literature.[21] QSTR model clearly suggested that all the lead molecules are non-toxic and noncarcinogenic (Table S5, ESI).

2.4 | AO/ErBr staining

The dual staining of acridine orange (AO) and ethidium bromide (EtBr) phenomenon speculates that AO penetrated normal and early apoptotic cells with intact membranes, fluorescing green. Ethidium bromide entered in damaged cells, such as late apoptotic and dead cells, emitting orange-red fluorescence via binding to DNA. The efficacy of ferrocenenylmethylamino functionalized amide inhibitor 5b to induce programmed cell death was observed prominent as a promising anti-proliferative agent in comparison to 4b and 1b (Figure 5). The apoptotic pattern observed after exposure of 4b was pre-eminent as compare to 1b. HepG2 cells were featured with apoptotic cell death after the exposure of 5b and 4b, whereas the morphological pattern of 1b inhibitor suggested secondary necrosis.

2.5 | Transcript analysis

Transcript analysis revealed that the expression level of cellular inhibitors of apoptosis 1 (cIAP1) was positively associated with TNFR1 in cancer survival. Activation of TNFR1, surface receptor, and cIAP1 amplification is commonly observed outline of cancer to promote cell proliferation. As expected, data of the present study (Figures S35–S37, ESI) suggested that inactivation of TNFR1 and depletion of cIAP1 expression inhibits the expression of p38MAPK and escort the cell for apoptosis. On the treatment of amide functionalized 2^0- and 3^0-aminomethylferrocene ligands to selected cell lines, cIAP1 expression decreased as compared to control. Expression of p38MAPK expression was also measured fold decrease after treatment that was in support of cIAP1 expression. On downregulation of p38MAPK, rate of proliferation decreased that would be in support of the cyclin dependent kinase (CDK) expression. Lower the expression of p38MAPK alters the cancerous cell physiology and triggers an antiproliferative cascade in cells. This phenomenon was supported by the expression of CDK, p53 and tubulin. Lower the expression of cyclin dependent kinase and tubulin, augment cell cycle arrest that induces programmed cell death in cells. The tumor suppressor p53 and its expression after the exposure of amide functionalized 2^0- and 3^0-aminomethylferrocene ligands were observed fold elevated that was supportive phenomenon for apoptosis induction in cancerous cell. Bcl2 family protein is a key regulator of programmed cell death. The expression of Bax, pro-apoptotic inducing member of Bcl2 family, showed fold increased, whereas the expression of anti-apoptotic member, Bcl2 expression

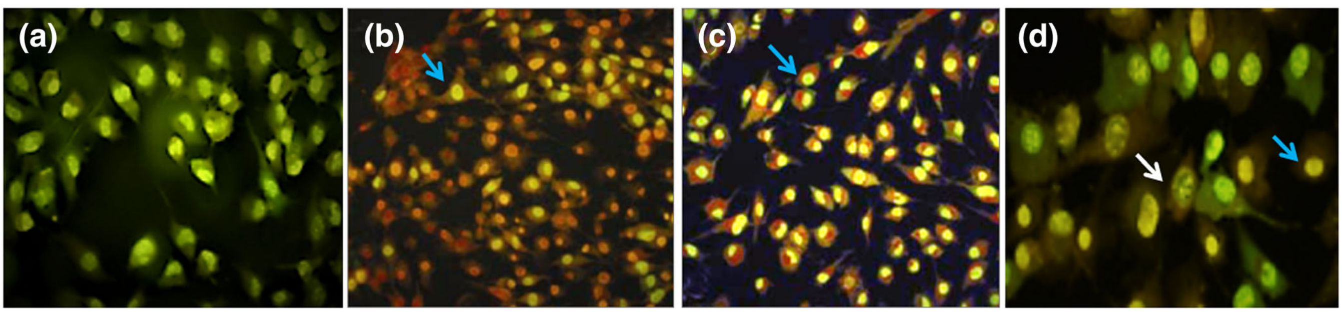

FIGURE 5 AO/ErBr staining on HepG2 cells. (a) Untreated cell stained by AO with more viable cell density; (b) 1b); (c) 4b); (d) 5b) Treated cell staining pattern by AO/EtBr. On treatment of 1b, 4b and 5b ligands to HepG2 cells apoptotic pattern of dual staining was observed. Cells stained green represent viable cells, whereas yellow staining represents early apoptotic cells (white arrow), and reddish or orange staining (blue arrow) represents late apoptotic cells

decreased after 24 h of treatment. The activity of caspase 9 is enhanced during apoptosis, which was observed fold upregulated after treatment. The change in the expression pattern of apoptosis transcript was prominent in comparison to cisplatin treatment. Cisplatin is considered to be drug resistant on exposure. There was no clear relation between cisplatin induced apoptosis through intrinsic Bcl2 and Bax expression and modulation of the Bcl-2/Bax ratio.[22] This was in correlation n with the present result of positive control cisplatin. In comparison to all the synthesized inhibitors, 4b has shown a most promising modulatory effect on transcript expression of cancerous cell lines. The transcript expression of TNFR1 was observed fold decreased after 4b treatment. The fold decreased expression of TNFαR1 was 2-fold in HepG2, 3.7-fold in MCF 7 and 2.93 in IMR 32 cells after 24-h treatment of 4b, whereas fold upregulated transcript expression of tumor suppressor gene p53 was 2.99-fold in HepG2, 2.23-fold in IMR32 and 2.5-fold in MCF 7 cells. The pattern of low expression of anti-apoptotic cell proliferation regulatory gene and upregulation of tumor suppressor gene was followed by 5b inhibitor as second most effective apoptosis inducer.

According to Pearsons's correlation analysis for HepG2 cells, the TNFR1 expression level was positively correlated with cIAP expression ($r = 0.695$, $P = 0.01$, 4b; $r = 0.703$, $P = 0.002$, 5b), whereas expression of Bcl2 and caspase 9 was negatively correlated ($r = -0.859$, $P = 0.001$, 4b; $r = -6.09$, $P = 0.009$, 5b). There was a positive correlation observed between caspase 9 and Bax expression ($r = 0.804$, $P = 0.005$, 4b; $r = 0.681$, $P = 0.002$).

2.6 | Annexin V/Propidium iodide assay

Annexin V/PI staining and flow cytometry were performed to investigate the cell death analysis after 24 h of 4b and 5b ligand treatment to HepG2 cells. According to our results displayed in Table 3, there was significant apoptotic cell death after the treatment of target ligand. Apoptotic (pro and late) death was accounted for 77.3% and 70.3% after 24 h of treatment of 4b and 5b, respectively. As shown, the cell population decreased in the live cell quadrangle (Q3) and increased in pro-apoptotic and apoptotic quadrangle (Q4 and Q2) (Figure 6). The PI positive cell was less in untreated control HepG2 cells. Results are in support of AO/EtBr staining where apoptotic cell were observed significantly. Evidently, with an increase in the expression of apoptosis initiator caspase 9, enhance the DNA fragmentation and loss the membrane integrity. Therefore, the binding efficiency of PI was increased and scored under apoptotic cell death.[23]

TABLE 3 Percent pattern of cell death of HepG2 cells after 24 h of targeted ligand treatment

Cell Pattern	Untreated(A) %	4b(B) %	5b(C) %
Live	78.4	19.2	28.2
Pro-apoptotic	8.1	58.2	53.2
Late apoptotic	11.3	19.1	17.1

2.7 | Protein expression analysis

Protein expression was measured to verify post-transcription/translation modification on exposure of 4b and 5b inhibitors. As shown in Figure 7a, inhibition of the TNFR1 protein expression in HepG2 cells was observed upon treatment with 4b and 5b inhibitors. Figure 7b revealed that level of TNFR1 protein decreased with increasing time of exposure of 4b and 5b. Western blot analysis shows down regulation of cIAP and phosphorylated p38MAPK on redundant of TNFR1 expression. cIAP1 deficiency sensitizes certain cell types to TNF induced programmed cell death. The phenomenon of the anticancer drug is to activate mitochondrial dependent pathway via releasing caspase 9 in apoptosis prone cancer cell.[24] TNFR1 dependent apoptosis, indicating that caspase-9 activation contributed to the activation of the caspase cascade and escort cancerous cell on death pathway via inhibiting proliferative marker like p38MAPK.[25] Moreover, on activation of caspase 9, mitochondria release IAP inhibitor and activate caspase-3. This, in turn, sensitizes neoplastic cells to apoptosis. The phenomenon of apoptosis is supported by the loss of protein expression of current study shown in Figure 7c,d, where cAIP and phosphorylated p38MAPK protein expression was downregulated.

2.8 | Mitochondrial membrane potential

Several apoptotic events occur in mitochondria, of which, the most significant event is the loss of mitochondrial membrane potential ($\Delta\Psi_M$).[26] JC-1 staining emits red fluorescence on J-aggregates with a normal $\Delta\Psi_M$ of mitochondria, whereas, on a decrease in red/green fluorescence intensity ratio marks mitochondrial depolarization.[26,27] On staining, significant shift in the fluorescence intensity ratio (towards green) in 4b and 5b treated HepG2 cells was observed (Figure 8). A fluorescence shift towards green was accounted higher on 5b treatment in comparison to 4b exposure to the cells. Evidently, amide

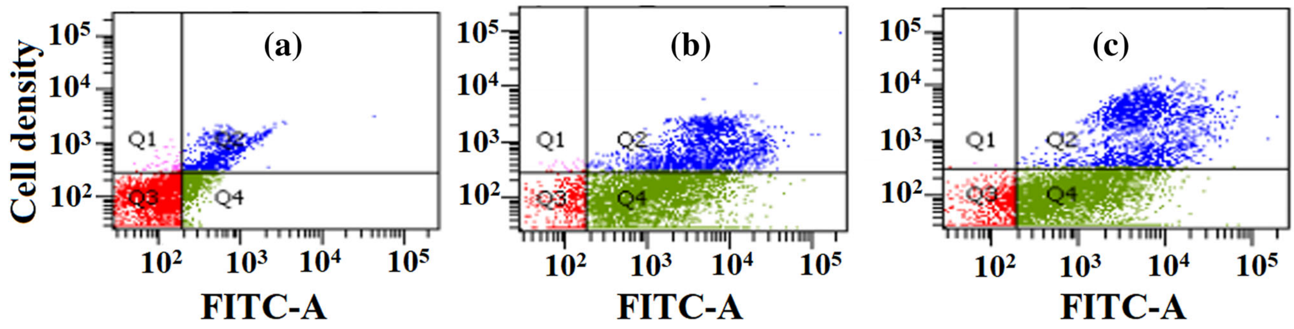

FIGURE 6 Fluorescent assorted cell sorting (FACS) for analysis of cell death using Annexin/PI staining after 24 h of treatment to HepG2 cells. (a) Untreated cells, (b) 4b ligand, and (c) 5b ligand treated HepG2 cells

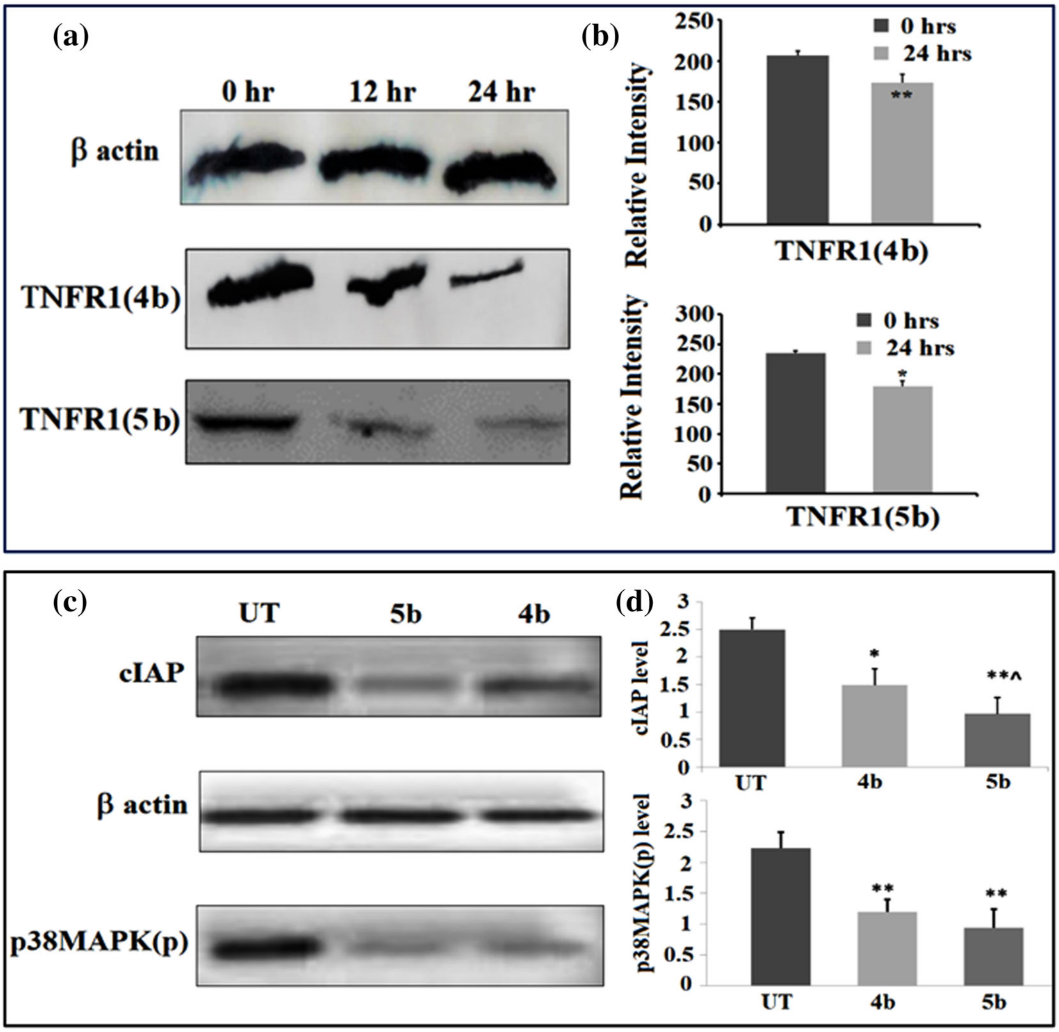

FIGURE 7 Western blot analysis of protein expression: (a) Blot of TNFR1 protein at different time interval on exposure of 4b and 5b inhibitors; (b) relative loss of protein level at 24 h; (c) western blot of cIAP and phopho-p38MAPK; (d) relative depletion of protein level at 24 h. UT—untreated cell at 0 h. * = *p* $p \leq 0.005$ ** = $p \leq 0.001$ in comparison with UT and ^ = $p \leq 0.005$ in comparison with 4b

functionalized 2^0- and 3^0-aminomethylferrocene inhibitors 4b and 5b hampered mitochondrial membrane potential via depolarization of the membrane. Loss of mitochondrial depolarization in HepG2 cells, suggesting that 4b and 5b alters mitochondrial respiration and insult the cells through ROS production. Our study

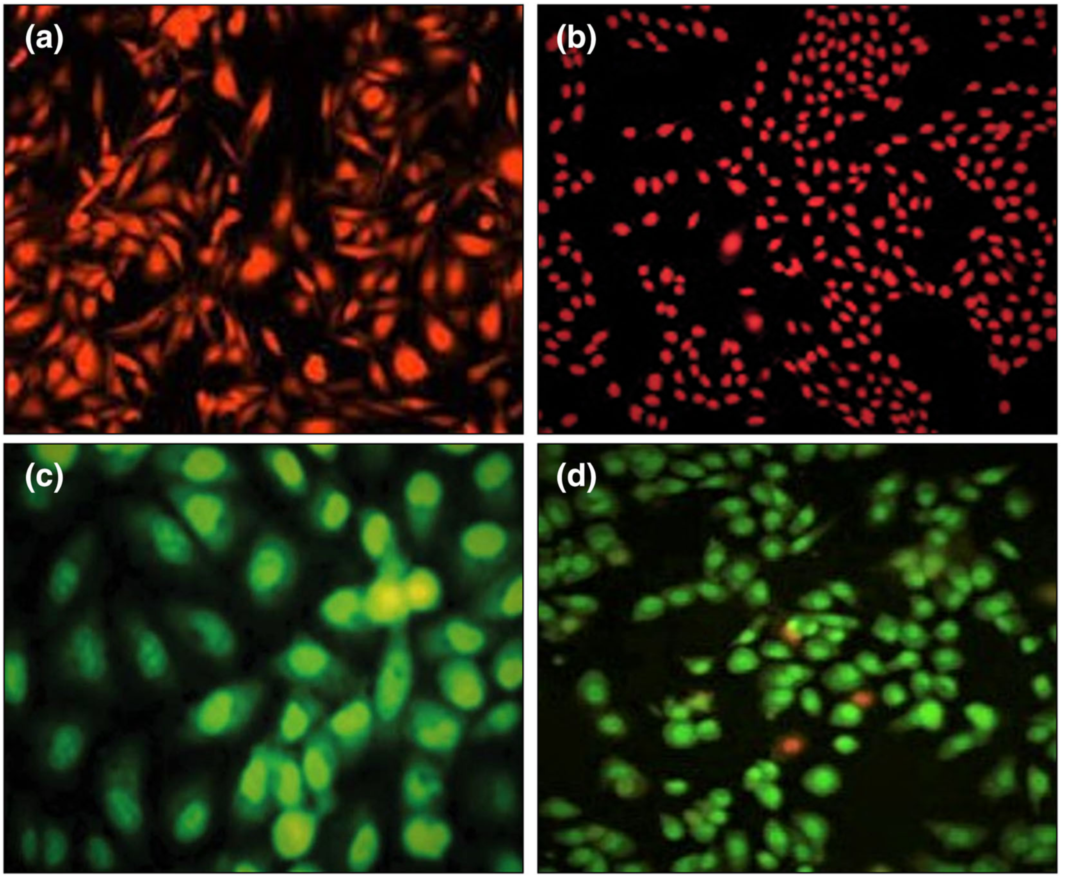

FIGURE 8 JC 1 staining of HepG2 cells to observe mitochondrial membrane potential ($\Delta\Psi_M$). (a) J aggregate at 0 h. (b) J aggregate at 24 h. (c) J monomers at 24 h after 5b exposure. (d) J monomers at 24 h after 4b exposure

corroborates previous notions that strengthening the relation of loss of mitochondrial membrane potential and apoptotic metabolic profile of cell can be exploited as prodrug chemotherapeutic property of ligand.[28] Loss of membrane potential was in support of gene expression pattern of caspase 9, Bcl2 and Bax. Over expression of Bax and down regulation of Bcl2 were measured after 4b and 5b treatment which is an applicable molecular event to hamper cell survival through membrane potential shift of mitochondria.

2.9 | Protein-ligand molecular docking

The manuscript characterizes the antineoplastic properties of amide functionalized 2^0- and 3^0-aminomethylferrocene ligands 1a-5a, 1b-5b to propose them as prodrug with potential to alter the inflammatory pathway. Molecular docking for protein-ligand studies have been performed to determine the binding mode of synthesized inhibitors 1a-5a, 1b-5b with the most probable sites of TNFα receptor. The Crystal contacts and hydrophobicity (Figure S48, ESI) of TNFα protein was elucidated by Ramachandran Plot (Figure S49, ESI). Dock scores for each ligand with different poses have been represented in Table 4. Based on dock score, it is clear that complexes 4b selectively bind to TNFR1 at the Tyr149 site and to 5b at the Gly121 sites more effectively than the other ligands. Binding interaction of 4b and 5b ligands with the TNFR1 protein is shown in Figure 9 while the interaction of other ligands is illustrated in the ESI (Figures S38–S45).

The analysis of molecular docking suggests that 4b and 5b might work as antagonist of TNFα, and bind to TNFR1 which change the configuration and inhibits binding of cIAP1 that alters the survival signaling of TNFR1 and induce cell death. Sacchi et al. have shown that derivatives of TNFα target effect on angiogenesis as well as shown reduced toxicity, as an antitumor agent in comparison to cisplatin, doxorubicin, paclitaxel and melphalan on some cancer like lymphoma, breast cancer.[29] Our dock results demonstrate that ligands 4b and 5b might be standardized as an effective prodrug for cancer therapeutics.

TABLE 4 TNF tyrosine residue and interaction of ligands with TNFα receptor

PDB Code	Ligand	Ligand interaction: Hydrogen Bonding	Ligand interaction: Hydrophobic interaction	Binding energy (Kcal/mol)
1tnf	1a	Tyrosine 119	Pro-117, Leu-120 and Leu-94	−5.33
1tnf	1b	Tyrosine 119	Pro-117	−5.97
1tnf	2a	Tyrosine 119	ILE-118, Ala-96, Leu-120 and Leu-94	−5.61
1tnf	2b	Tyrosine 119	Pro-117, and Leu-94	−6.33
1tnf	3a	Tyrosine 119	ILE-118, Ala-96, Leu-120 and Leu-94	−4.95
1tnf	3b	Tyrosine 119	ILE-118, Ala-96, Leu-120, Leu-94 and GLy-121	−5.89
1tnf	4a	Tyrosine 119	ILE-118, Ala-96, Leu-120, Leu-94	−5.40
1tnf	4b	Tyrosine 119	Leu-120 and Leu-94 and Pro-117	−6.55
1tnf	5a	Tyrosine 119	Leu-120 and ILeu-118 and Pro-117	−5.06
1tnf	5b	Glycine 121	Tyrosine-119, LYS-98 ILE-118, Ala-96, Leu-120	−6.34

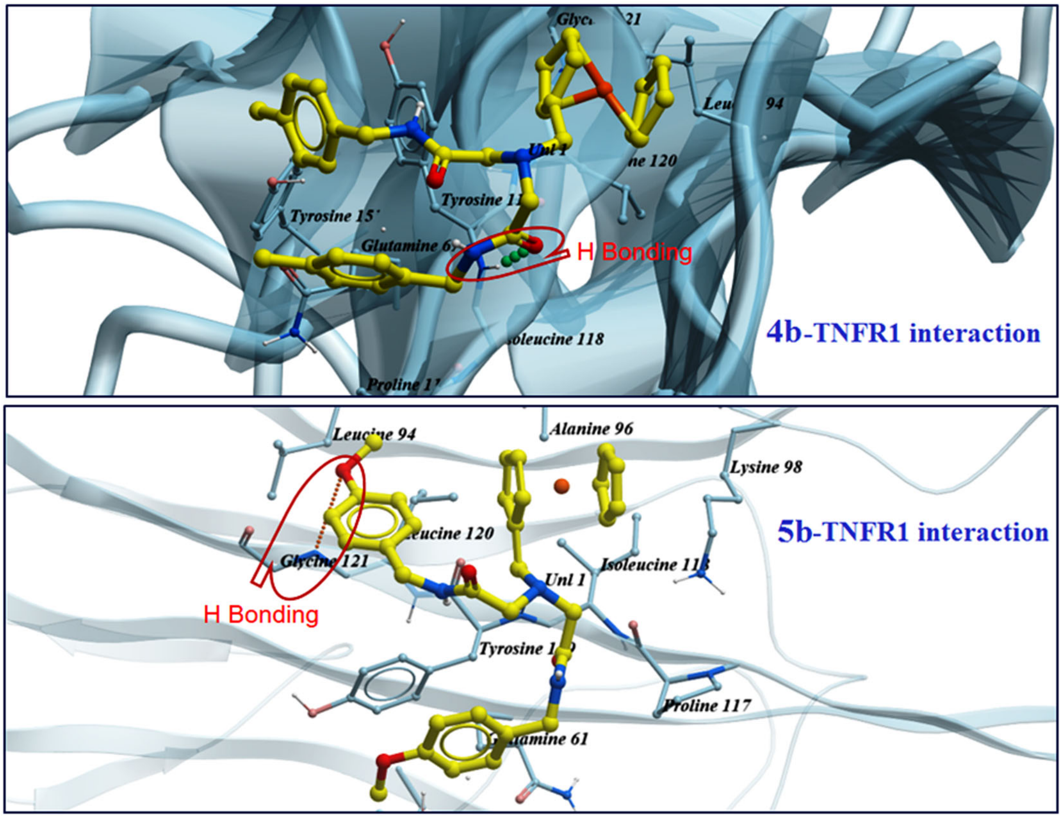

FIGURE 9 Binding of inhibitors 4b and 5b with TNFα receptor

3 | CONCLUSIONS

This study allows us to conclude that many of the newly synthesized ferrocenylmethyamine derivatives showed potent inhibition of cell growth in low μM concentrations against various carcinoma cell lines of human origin. For instance, inhibitor 5b shows highest inhibition (IC_{50}: 2.1 ± 0.41 μM), which is 15 fold, while 2b (IC_{50}: 10.49 ± 0.37 μM) and 4b (IC_{50}: 11.49 ± 0.07 μM) show ~3 fold better inhibition against MCF7 as compared to cisplatin (IC_{50}: 32.41 ± 1.5 μM). Moreover, bis-amide inhibitor 4b (IC_{50}:10.39 ± 0.30 μM) and 5b (IC_{50}: 16.95 ± 0.15 μM) show ~3–2 fold better inhibition against IMR32 than the reference (IC_{50}: 29.6 ± 1.26 μM). Also, inhibitors 1a (IC_{50}: 13.19 ± 0.17 μM), 1b (7.25 ± 0.11 μM), 2b (IC_{50}: 14.60 ± 0.08 μM), 3b (IC_{50}:

13.74 ± 0.05 μM) and 5b (8.66 ± 0.21 μM) have shown the better potency against HepG2 than cisplatin (IC_{50}: 24.3 ± 1.7 μM). The IC_{50} values of some of these compounds are found to be comparable with a number of recently reported high molecular weight organometallic compounds;[21a] however, they showed better activity than the ferrocence-glycine/L-alanine hybrids against MCF-7 cells (Table S3).[21b] Highest dock score of 5b-TNFR1 suggested that the ligand 5b has a modulatory effect on TNF*α* receptor mediated signaling pathway, which is indeed one of the known pathways involved in cancer progression and metastasis. Evidently, the loss in the expression from cancer cells induces TNFα dependent apoptosis. The reduced phosphorylation of p38MAPK hampers cell proliferation via downregulating CDK and up regulating p53 and thereby enhances the apoptosis in selected cancer cells. Moreover, loss of cIAP activates caspase cascade and alters mitochondrial membrane potential. The synergistic effect of amido, amino and ferrocenyl groups present in the molecular framework evidently enhanced the potentials of synthesized amino ligands as TNFR1 inhibitors and projects them as a persuasive antitumor agent. In general, commercially and industrially important as well as pharmaceutically relevant amines were synthesized in good yields. The future aspect of present amines is to functionalize amino handles of amide functionalized 2^0-aminomethylferrocene (1a-5a) into diverse bioactive ligands.

3.1 | Experimental section

Material and physical measurements. All amines were synthesized following literature procedure. Ferrocenylmethylamine, *α*-chloroamide precursors were synthesized by a modified literature procedure.[17] Reactions and manipulations were performed in the atmosphere of nitrogen. All the chemicals and solvents used in this work were of laboratory grade available at various commercial sources and used without further purification. Thin Layer Chromatography was performed on Merck 60F254 aluminium coated plates. FT-IR (KBr pellets) spectra were recorded in the 4000–400 cm^{-1} range using a Perkin-Elmer FT-IR spectrometer. The NMR experiments were carried out on a Bruker AV-III 400-MHz spectrometer in $CDCl_3$ solvents as per the solubility and chemical shifts are reported in parts per million (ppm). UV–visible absorption spectra were recorded on a JASCO V-730 UV–visible spectrophotometer Fluorescence was recorded on JASCO make spectrofluorometer model FP-8200. TGA/DTA plots were obtained using SII TG/DTA 6300 in flowing N_2 with a heating rate of 10°C min^{-1}.

General procedure for the synthesis of 2-(ferrocenylmethylamino)-N-alkylacetamide (1a-5a). N-cyclohexyl-2-iodoacetamide was prepared by reacting N-cyclohexyl-2-chloroacetamide with KI in acetone and it was subsequently utilized in the synthesis of corresponding 2-(ferrocenylmethylamino)-*N*-alkylacetam ides. ca *N*-benzyl-2-iodoacetamide (0.289 g, 1.05 mmol), *N*-cyclohexyl-2-iodoacetamide (0.280 g, 1.05 mmol), *N*-furfuryl-2-iodoacetamide (0.278 g, 1.05 mmol), *N*-4-methylbenzyl-2-iodoacetamide (0.303 g, 1.05 mmol) or *N*-4-methoxybenzyl-2-iodoacetamide (0.320 g, 1.05 mmol) was added portion wise to the solution of amino methyl ferrocene (0.215 g, 1.0 mmol) in 25 ml of $CHCl_3$ containing 3–4 drops of Et_3N. The reaction mixture was reflux for 3 h. The progress of the reaction was monitored by thin layer chromatography and ninhydrin. The reaction mixture was cooled at room temperature and solvent was removed under vacuum. Distilled water was added in the solid residue and the crude product was extracted by using dichloromethane. It was dried over Na_2SO_4 for 4 h, and the solvent was removed by rotator evaporator. The residue was column chromatographed to give pale yellow coloured thick liquid products 1a-5a in 60%–70% yield. The reaction could not complete even after prolonged refluxing, which leads to decomposition.

General procedure for the synthesis of 2, 2′-(ferrocenylmethylazanediyl)bis(N-alkylacetamide) (1b-5b). *N*-benzyl-2-iodoacetamide (0.564 g, 2.05 mmol), *N*-cyclohexyl-2-iodoacetamide (0.547 g, 2.05 mmol), *N*-furfuryl-2-iodoacetamide (0.543 g, 2.05 mmol), *N*-4-methylbenzyl-2-iodoacetamide (0.592 g, 2.05 mmol) or *N*-4-methoxybenzyl-2-iodoacetamide (0.625 g, 2.05 mmol) was added portion wise to the solution of amino methyl ferrocene (0.215 g, 1 mmol) in 25 ml of CH_3CN containing Na_2CO_3 (0.265 g, 2.5 mmol). The reaction mixture was reflux for 6 h. The similar workup procedure was adopted as descried earlier to give yellow coloured solid products 1b-5b in 80%–90% yield.

2-(ferrocenylmethylamino)-N-benzylacetamide (1a). Yellow thick liquid; MW 362. Yield: ~235 mg, 65%. Anal. Calcd for [$C_{20}H_{22}FeN_2O$]: C, 66.31; H, 6.12; N, 7.73. Found: C, 66.41; H, 6.22; N, 7.82. ^1H NMR (400 MHz, $CDCl_3$) δ ppm: 7.74 (s, 1H, -N*H*CO); 7.28–7.36 (m, 5H, *Ph*); 4.44 (d, *J* = 5.6 Hz, 2H, -CH_2CO); 4.14–4.43 (m, 9H, *Fc*); 3.64 (s, 2H, -CH_2Ph); 3.49 (s, 2H, -CH_2Fc). ^{13}C NMR (400 MHz, $CDCl_3$) δ ppm: 176.5, 169.3, 137.9, 128.6, 127.7, 127.5, 82.1, 68.6, 50.2, 48.3, 43.2. IR (KBr, cm^{-1}): 3209 (N-H), 3,028(C-H), 2835 (C-H), 2603 (C-H), 1681 (C=O), 1531, 1392, 1269, 1103, 1026, 894, 698, 659, 497, 482.

2, 2′-(ferrocenylmethylazanediyl)bis(*N*-benzylacetamide) (1b). Yellow solid; MW 509. Yield: ~417 mg, 82%. Melting point: 142°C. Anal. Calcd for

[$C_{29}H_{31}FeN_3O_2$]: C, 68.37; H, 6.13; N, 8.25. Found: C, 68.51; H, 6.20; N, 8.38. ^{1}H NMR (400 MHz, $CDCl_3$) δ ppm: 7.62(s, 2H, -N*H*CO); 6.94–7.37(m, 10H, Ph); 4.07–4.38 (m, 9H, *Fc*); 4.45 (s, 4H, -C*H*$_2$CO); 3.51(s, 4H, -C*H*$_2$Ph); 3.17 (2H, s, –C*H*$_2$ Fc). ^{13}C NMR (400 MHz, $CDCl_3$) δ ppm: 170.1, 138.1, 128.7, 127.7, 127.5, 69.8, 68.6, 58.2, 55.1, 43.2, 30.9. IR (KBr, cm^{-1}): 3448 (N-H), 3313(N-H), 2962 (C-H), 2920 (C-H), 1670 (C=O), 1639 (C=O), 1539, 1504, 1450, 1427, 1261, 1103, 1022, 802, 698, 482.

2-(ferrocenylmethylamino)-N-cyclohexylacetamide (2a). Yellow oily liquid; MW 354. Yield: ~212 mg, 60%. Anal. Calcd for [$C_{19}H_{26}FeN_2O$]: C, 64.42; H, 7.40; N, 7.91. Found: C, 64.50; H, 7.46; N, 7.98. ^{1}H NMR (400 MHz, $CDCl_3$) δ ppm: 6.51 (s, 1H, -N*H*CO); 4.14–4.22 (m, 9H, *Fc*); 3.62 (m, 1H, *Cy*); 3.40 (s, 2H, –C*H*$_2$Fc); 3.20 (s, 2H, –C*H*$_2$CO); 2.08 (s, 1H, NH(-C*H*$_2$Fc)) 1.19–1.90 (m, 10H, *Cy*). ^{13}C NMR (400 MHz, $CDCl_3$) δ, ppm 168.1, 81.0, 68.6, 33.0, 32.8, 30.9, 25.4, 24.7, 21.6. IR (KBr, cm^{-1}): 471 (N-H), 3163(C-H), 2800 (C-H), 1666(C=O), 1550, 1404, 1234, 1103, 1126, 910, 810, 648, 439.

2, 2′-(ferrocenylmethylazanediyl)bis(*N*-cyclohexylacetamide) (2b). Yellow solid; MW 493. Yield: ~419 mg, 85%. Melting point: 153°C. Anal. Calcd for [$C_{27}H_{39}FeN_3O_2$]: C, 65.72; H, 7.97; N, 8.52. Found: C, 65.79; H, 8.06; N, 8.65. ^{1}H NMR (400 MHz, $CDCl_3$) δ ppm: 6.51 (s, 2H, N*H*CO); 4.12–4.17(m, 9H, *Fc*); 3.78 (m, 2H, *Cy*); 3.54 (s, 2H,–C*H*$_2$ Fc); 3.12 (s, 4H,–C*H*$_2$ CO); 1.12–1.91(m, 20H, *Cy*). ^{13}C NMR (400 MHz, $CDCl_3$) δ, ppm 169.3, 81.8, 69.8, 68.6, 58.2, 55.1, 47.8, 33.08, 30.9, 25.4, 24.7. IR (KBr, cm^{-1}): 3321(N-H), 2,931 (C-H), 2846 (C-H), 1681(C=O), 1643(C=O), 1535, 1450, 1315, 1253, 1103, 1026, 817,759, 493, 478.

2-(ferrocenylmethylamino)-N-furfurylacetamide (3a). Yellow oily liquid; MW 352. Yield: ~222 mg, 63%. Anal. Calcd for [$C_{18}H_{20}FeN_2O_2$]: C, 61.38; H, 5.72; N, 7.95. Found: C, 61.47; H, 5.90; N, 8.08. ^{1}H NMR (400 MHz, $CDCl_3$) δ ppm: 7.64 (s, 1H, N*H*CO); 7.28 (d, *J* = 0.8 Hz, 1H, *furyl*); 6.34 (t, *J* = 2 Hz, 1H, *furyl*); 6.23 (d, *J* = 2.8 Hz, 1H, *furyl*); 4.14–4.19 (m, 9H, *Fc*); 4.44 (s, 2H, -C*H*$_2$furyl); 3.59 (2H, s, –C*H*$_2$Fc); 3.42(s, 2H, –C*H*$_2$CO) ^{13}C NMR (400 MHz, $CDCl_3$) δppm: 170.0, 151.1, 142.2, 110.4, 107.4, 83.3, 68.5, 50.6, 48.4, 36.1. IR (KBr, cm^{-1}): 3201 (N-H), 2885 (C-H), 2816 (C-H), 1681(C=O), 1527, 1338, 1265, 1018, 887, 810, 748, 655, 486.

2, 2′-(ferrocenylmethylazanediyl)bis(*N*-furfurylacetamide) (3b). Yellow solid; MW 489. Yield: ~430 mg, 88%. Melting point: 132°C. Anal. Calcd for [$C_{25}H_{27}FeN_3O_4$]: C, 61.36; H, 5.56; N, 8.59. Found: C, 61.44; H, 5.61; N, 8.63. ^{1}H NMR (400 MHz, $CDCl_3$) δ ppm: 7.37 (d, *J* = 0.8 Hz, 2H, *furyl*); 6.89 (s, 2H, N*H*CO); 6.34 (t, *J* = 1.2 Hz, 2H, *furyl*); 6.23(s, *J* = 2.8 Hz, 2H, *furyl*); 4.42 (s, 4H, -C*H*$_2$furyl); 4.05–4.12 (m, 9H, *Fc*); 3.50 (2H, s, –C*H*$_2$Fc); 3.17(s, 4H, –C*H*$_2$CO). ^{13}C NMR (400 MHz, $CDCl_3$) δppm 170.1, 151.1, 142.1, 110.5, 107.3, 81.4, 68.6, 58.0, 54.9, 36.1, 30.9. IR (KBr, cm^{-1}): 3340 (N-H), 2,920 (C-H), 2850 (C-H), 1674 (C=O), 1651 (C=O), 1508, 1423, 1356, 1284, 1203, 1145, 1107, 1018, 756, 740, 474.

2-(ferrocenylmethylamino)-N-paramethylacetamide (4a). Yellow oily liquid; MW 376. Yield: ~229 mg, 61%. Anal. Calcd for [$C_{21}H_{24}FeN_2O$]: C, 67.03; H, 6.43; N, 7.44. Found: C, 67.12; H, 6.49; N, 7.53 ^{1}H NMR (400 MHz, $CDCl_3$) δ ppm: 7.50(s, 1H, -N*H*CO); 7.13–7.49 (m, 4H, *Ph*); 4.42 (d, *J* = 6 Hz, 2H, -C*H*$_2$CO); 4.08–4.16 (m, 9H, *Fc*); 3.47 (s, 2H, -C*H*$_2$Ph); 3.33(s, 2H, -C*H*$_2$Fc); 2.34(s, 3H, C*H*$_3$). ^{13}C NMR (400 MHz, $CDCl_3$) δ ppm: 170.5, 137.1, 135.1, 129.3, 127.7, 68.5, 51.0, 48.9, 42.8, 21.1. IR (KBr, cm^{-1}): 3317 (N-H), 3086 (C-H), 3008 (C-H), 2835 (C-H), 2823 (C-H), 1658 (C=O), 1519, 1427, 1357, 1257, 1103, 1026, 810, 478.

2,2′-(ferrocenylmethylazanediyl)bis(*N*-paramethylacetamide) (4b). Yellow solid; MW 537. Yield: ~483 mg, 90%. Melting point: 123°C. Anal. Calcd for [$C_{31}H_{35}FeN_3O_2$]: C, 69.27; H, 6.56; N, 7.82. Found: C, 69.33; H, 6.61; N, 7.87. ^{1}H NMR (400 MHz, $CDCl_3$) δ ppm: 7.141(m, 5H, *Ph*); 6.9(s, 1H, -N*H*CO); 3.98–4.35 (m, 9H, *Fc*); 4.35 (s, 2H, -C*H*$_2$CO); 3.56 (s, 2H, -C*H*$_2$Ph); 3.19 (s, 2H, -C*H*$_2$Fc); 2.36 (s, 3H, C*H*$_3$). ^{13}C NMR (400 MHz, $CDCl_3$) δ ppm: 166.7, 137.3, 134.3, 129.4, 127.8, 44.2, 21.1. IR (KBr, cm^{-1}): 3360 (N-H), 3321(C-H), 2920 (C-H), 2854 (C-H), 1670 (C=O), 1639 (C=O), 1535, 1431, 1257, 1107, 1026, 840, 802, 752, 470.

2-(ferrocenylmethylamino)-N-paramethoxybenzylacetamide (5a). Yellow oily liquid; MW 392. Yield: ~243 mg, 62%. Anal. Calcd for [$C_{21}H_{24}FeN_2O_2$]: C, 64.30; H, 6.17; N, 7.14. Found: C, 64.35; H, 6.24; N, 7.20. ^{1}H NMR (400 MHz, $CDCl_3$) δ ppm: 7.50(s, 1H, -NHCO); 7.2(d, *J* = 8.8 Hz, 2H, Bz); 6.8(d, *J* = 8.7 Hz, 2H, *Ph*); 6.84–4.30 (d, *J* = 6.0 Hz, 2H, -C*H*$_2$CO); 4.01–4.32 (m, 9H, *Fc*); 3.96 (s, 3H, -OC*H*$_3$); 3.74 (s, 2H, -C*H*$_2$Ph); 3.23 (s, 2H,–C*H*$_2$Fc). ^{13}C NMR (400 MHz, $CDCl_3$) δ ppm: 170.7, 158.8, 130.5, 129.1, 114.0, 84.5, 81.6, 68.5, 55.3, 51.2, 48.8, 42.4. IR (KBr, cm^{-1}): 3308(N-H), 3081(C-H), 2931(C-H), 2834(C-H), 1655(C=O), 1513, 1460, 1301, 1247, 1176, 1105, 1133, 1001, 818, 484.

2,2′-(ferrocenylmethylazanediyl) bis(*N*-paramethoxybenzylacetamide) (5b). Yellow solid; MW 569. Yield: ~523 mg, 92%. Melting point: 170°C. Anal. Calcd for [$C_{31}H_{35}FeN_3O_4$]: C, 65.38; H, 6.20; N, 7.38. Found: C, 65.47; H, 6.29; N, 7.42. ^{1}H NMR (400 MHz, $CDCl_3$) δ ppm: 7.59 (s, 2H, -N*H*CO); 7.2(d, *J* = 8.8 Hz, 2H, *Ph*); 7.1 (d, *J* = 8.7 Hz, 2H, *Ph*); 6.84–7.27 (m, 4H, *Ph*); 4.35 (d, 4H, -C*H*$_2$CO); 4.05–4.30 (m, 9H, *Fc*); 3.97 (s, 6H, -OC*H*$_3$); 3.79 (s, 4H, -C*H*$_2$Ph); 3.15 (s, 2H,–C*H*$_2$ Fc). ^{13}C NMR (400 MHz, $CDCl_3$) δ ppm: 170.0, 138.1, 128.7, 127.7, 127.5, 69.8, 68.6, 58.2, 55.1, 43.2, 30.9. IR (KBr, cm^{-1}):

3317(N-H), 3008(C-H), 2994(C-H), 2877(C-H), 1607 (C=O), 1643(C=O), 1512, 1427, 1350, 1259, 1172, 1111, 1026, 840, 817, 594, 516, 478.

ESI. ^{1}H, ^{13}C NMR, IR, UV–visible, fluorscenec spectra, X-ray data collection and refinement statistics, figures displaying propensity of ligands to form H-bonding inetarctions, experimental protocols and additional figures related to biology, computational, molecular docking and Hirshfeld surface analysis are embedded in the ESI.

Crystallographic information (CIF). CCDC No. 1915118 for 3a.CH_3COOH, 1915119 for 3b, 1915120 for 1a. $2HI.\ H_2O$, 1915121 for 4b, 1915123 for 5b.

ACKNOWLEDGEMENTS

V. K. S. acknowledges Science and Engineering Research Board, New Delhi, India (Reference No. EMR/2016/003172) for the financial support. We also thank the DST-PURSE and Fist, New Delhi, for the projects under which the single crystal X-ray diffractometer and NMR instruments were acquired in the Faculty of Science.

AUTHOR CONTRIBUTIONS

Chirag Savani: Conceptualization; data curation; formal analysis; investigation; software. **Hetal Roy:** Data curation; investigation; methodology; software; validation. **Sanjay Verma:** Data curation; formal analysis; investigation; software. **Dushyanth Vennapu:** Data curation; formal analysis; investigation; software. **Vinay Singh:** Conceptualization; funding acquisition; investigation; project administration; supervision.

DATA AVAILABILITY STATEMENT

Data sharing not applicable as no new data generated.

ORCID

Chirag J. Savani https://orcid.org/0000-0002-1918-3498
Hetal Roy https://orcid.org/0000-0001-7899-1930
Sanjay K. Verma https://orcid.org/0000-0002-4445-1271
Dushyanth R. Vennapu https://orcid.org/0000-0002-9524-0837
Vinay K. Singh https://orcid.org/0000-0002-7496-1029

REFERENCES

[1] a)T. J. Kealy, P. L. Pauson, *Nature* **1951**, *168*, 1039. b)S. A. Miller, J. A. Tebboth, J. F. Tremaine, *J. Chem. Soc.* **1952**, 632.
[2] a)D. Astruc, *Eur. J. Inorg. Chem.* **2017**, *2017*, 6. b)K. Heinze, H. Lang, *Organometallics* **2013**, *32*, 5623.
[3] a)R. Horikoshi, T. Mochida, *Eur. J. Inorg. Chem.* **2010**, *2010*, 5355. b)R. L. N. Hailes, A. M. Oliver, J. Gwyther, G. R. Whittell, I. Manners, *Chem. Soc. Rev.* **2016**, *45*, 5358.
[4] a)L. E. Wilson, C. Hassenrück, R. F. Winter, A. J. P. White, T. Albrecht, N. J. Long, *Eur. J. Inorg. Chem.* **2017**, *2017*, 496. b)I. Baumgardt, H. Butenschön, *Eur. J. Org. Chem.* **2010**, *2010*, 1076.
[5] H. Takashima, Y. Inagaki, H. Momma, E. Kwon, K. Yamaguchi, W. Setaka, *Organometallics* **2018**, *37*, 1501.
[6] P. Mathur, V. K. Singh, S. M. Mobin, C. Srinivasu, R. Trivedi, A. K. Bhunia, V. G. Puranik, *Organometallics* **2005**, *24*, 367.
[7] a)R. C. J. Atkinson, V. C. Gibson, N. J. Long, *Chem. Soc. Rev.* **2004**, *33*, 313. b)L. -X. Dai, T. Tu, S. -L. You, W. -P. Deng, X.-L. Hou, *Acc. Chem. Res.* **2003**, *36*, 659. c)R. G. Arrayás, J. Adrio, C. Carretero, *Angew. Chem., Int. Ed.* **2006**, *45*, 7674. d)P. Steffen, C. Unkelbach, M. Christmann, W. Hiller, C. Strohmann, *Angew. Chem., Int. Ed.* **2013**, *52*, 9836.
[8] a)M. Patra, G. Gasser, *Nat. Rev. Chem.* **2017**, *1*, 66. b)B. Albada, N. Metzler-Nolte, *Chem. Rev.* **2016**, *116*, 11797. c)K. D. Mjos, C. Orvig, *Chem. Rev.* **2014**, *114*, 4540. d)D. R. van Staveren, N. Metzler-Nolte, *Chem. Rev.* **2004**, *104*, 5931.
[9] a)H. Z. Zhang, S. Kasibhatla, J. Kuemmerle, W. Kemnitzer, K. Ollis-Mason, L. Qiu, C. Crogan-Grundy, B. Tseng, J. Drewe, S. X. Cai, *J. Med. Chem.* **2005**, *48*, 5215. b)A. Hunold, H. G. Schmalz, L. Kater, B. Bonitzki, P. A. Jesse, *J. Cancer Res. Clin. Oncol.* **2010**, *137*, 639.
[10] a) H. Helen, M. Paul, J. Elmar, Veldwijk Marlon; European Patent, No. EP 2 497 775 A1, **2012**. b)C. G. Hartinger, P. Dyson, *Chem. Soc. Rev.* **2009**, *38*, 391.
[11] S. K. Verma, V. K. Singh, *J. Organomet. Chem.* **2015**, 791. 214-224 *and the references cited in*
[12] G. Jaouen, A. Vessieres, S. Top, *Chem. Soc. Rev.* **2015**, *44*, 8802.
[13] a)Y. Zhang, K. T. Zhao, S. G. Fox, J. Kim, D. R. Kirsch, R. J. Ferrante, R. I. Morimoto, R. B. Silverman, *J. Med. Chem.* **2015**, *58*, 5942. b)V. K. Singh, R. Kadu, H. Roy, *Eur. J. Med. Chem.* **2014**, *74*, 552.
[14] S. Luo, P. Li, S. Li, Z. Du, X. Hu, Y. Fu, Z. Zhang, *Mol. Pharmaceutics* **2017**, *14*, 1771.
[15] S. N. Rao, D. C. Mohan, S. Adimurthy, *RSC Adv.* **2015**, *5*, 95313.
[16] X. Peng, Z. Sun, P. Kuang, L. Li, J. Chen, *Org. Lett.* **2020**, *22*, 5789.
[17] R. Kadu, H. Roy, V. K. Singh, *Appl. Organomet. Chem.* **2015**, *29*, 746.
[18] E. Assadian, H. Dezhampanah, E. Seydi, J. Pourahmad, *J. Biochem. Mol. Toxicol.* **2019**, *33*, e22303.
[19] S. Bittner, C. Meenakshi, G. Temtsin, *Tetrahedron* **2001**, *57*, 7423.
[20] A. Daina, V. Zoete, *ChemMedChem* **2016**, *11*, 1117.
[21] a)M. Odachowski, C. Marschner, B. Blom, *Eur. J. Med. Chem.* **2020**, *204*, 112613. b)R. Wang, H. Chen, W. Yan, M. Zheng, T. Zhang, Y. Zhang, *Eur. J. Med. Chem.* **2020**, *190*, 112109.
[22] a)A. Mandic, V. Viktorsson, M. Varsanyi, J. Hansson, S. Linder, M. C. Shoshan, *Nat. Genet.* **2001**, *27*, 86. b)H. Burger, K. Nooter, A. Boersma, C. Kortland, G. Stoter, *Br. J. Cancer* **1998**, *77*, 1562.
[23] S. Pietkiewicz, J. H. Schmidt, N. I. Lavrik, *J. Immunol. Methods* **2015**, *42*, 399.
[24] M. V. Blagosklonny, *Oncogene* **2004**, *23*, 2967.
[25] M. A. McDonnell, D. Wang, S. M. Khan, H. M. G. Vander, A. Kelekar, *Cell Death Differ.* **2003**, *10*, 1005.
[26] F. Sivandzade, A. Bhalerao, L. Cucullo, *Bio-Protoc.* **2019**, *9*, e3128.
[27] L. D. Zorova, V. A. Popkov, E. Y. Plotnikov, D. N. Silachev, I. B. Pevzner, S. S. Jankauskas, V. A. Babenko, S. D. Zorov,

A. V. Balakireva, M. Juhaszova, S. J. Sollott, D. B. Zorov, *Anal. Biochem.* **2018**, *552*, 50.
[28] R. Jitschin, A. D. Hofmann, H. Bruns, A. Giebl, J. Bricks, J. Berger, *Blood* **2014**, *123*, 2663.
[29] A. Sacchi, A. Gasparri, C. Gallo-Stampino, S. Toma, F. Curnis, A. Corti, *Clin. Cancer Res.* **2006**, *12*, 175.

SUPPORTING INFORMATION

Additional supporting information may be found online in the Supporting Information section at the end of this article.

How to cite this article: Savani CJ, Roy H, Verma SK, Vennapu DR, Singh VK. Synthesis, characterization and evaluation of novel ferrocenylmethylamine derivatives as cytotoxic agents. *Appl Organomet Chem*. 2021;e6137. https://doi.org/10.1002/aoc.6137